第 34 卷第 4 期
2015 年 8 月

红 外 与 毫 米 波 学 报
J. Infrared Millim. Waves

Vol. 34, No. 4
August, 2015

文章编号: 1001 - 9014(2015)04 - 0411 - 09

DOI:10.11972/j.issn.1001 - 9014.2015.04.006

A novel unified multispectral statistical algorithm for detecting dim point target in single frame IR image

LIU Da, LI Jian-Xun

(Institute of Information and Control, School of Information and Control, Shanghai Jiao Tong University, Shanghai 200030, China)

Abstract: Target spectral signature is modeled firstly based on the thermal radiation theory and a multispectral background suppression approach is given. An experimentally justified assumption is made that the probability density functions (PDFs) of the feature vector can be modeled as Gaussian random process, and then a new unifying radiation intensity and radiation spectral signature (URIS) detector is developed. Finally, performance analyses based on a set of multispectral imagery and receiver operating characteristic (ROC) curves are presented. According to the experimental results, the URIS method can successfully detect dim point target in rather low signal-to-noise condition.

Key words: IR image, target detection, data Cube, multispectral, low SNR, statistical decision
PACS: 42.30.-d

一种新的单帧红外弱点目标多光谱联合统计检测方法

刘 达, 李建勋
(上海交通大学 电子信息与电气工程学院,上海 200030)

摘要:首先基于红外物理基本理论建立目标光谱模型,并利用图像时域及空域相关性建立多光谱背静抑制算法移除缓慢变化背景.通过实验统计方法将残差图像样本点特征概率分布近似为正态分布.基于此假设,提出了一种新的基于目标辐射强度和光谱特征的联合检测方法.最后,通过图像仿真和 ROC 曲线分析算法性能,试验结果表明,此方法能够在低信噪比情况下成功检测弱小点目标.

关 键 词:红外图像; 目标检测; 数据立方体; 多光谱; 低信噪比; 统计决策

中图分类号:TP391.4 **文献标识码**:A

Introduction

During the past few years, analysis of hyperspectral and multispectral imagery has played an increasingly important role in many fields, such as: medical application[1], environment monitoring[2], crop health estimation[3], targets detection[4].

In multispectral images, spectral signature is the scientific descriptions of the detectable and recognizable infrared wavelengths. It represents the infrared radiation characteristics and reveals the intrinsic property of target and background. Utilizing such wealth of spectral and spatial information greatly improves the performance of the target detection and recognition, expands the traditional detection technology to a new frontier.

Spectral target detection and recognition algorithms are broadly classified into spectrum matching algorithm and anomaly spectrum algorithm. The main difference between the two approaches is that if there is any prior information. (i) Spectrum matching approach determines whether a match exists between the reference signature and the spectral signature of the image pixels. (ii) Anomaly spectrum algorithm identifies the scene pixels as the potential targets whose signature do not fit the background model.

Reference[5] points out that, multispectral technology has become the main development trend of the infrared detection technology in the future. The pioneer work in

Received date: 2014 - 05 - 07, **revised date**: 2015 - 06 - 02 **收稿日期**:2014 - 05 - 07, **修回日期**:2015 - 06 - 02
Foundation items:Supported by National Natural Science Foundation of China(61175008)
Biography: LIU Da(1986-), male, Changchun, Jilin province, Ph. D. Research area involves Multispectral image processing and pattern recognition. E-mail: oliver8641@sjtu.edu.cn

this field can be traced to 1985; Margalit and Reed put forward a constant false alarm rate (CFAR) adaptive target detection algorithm using correlated images in Ref. [6]. In 1990, Reed and Yu X. proposed an adaptive multiple-band CFAR algorithm to detect targets with unknown spectral distribution in Ref. [7]. Harsanyi presented orthogonal subspace projection (OSP) and constrained energy minimization (CEM) algorithms in 1994[8]. The most basic and prevalent algorithm for multispectral imagery target detection is so called spectral angle mapper (SAM) proposed by Richards and Jia in 1999 [9]. SAM algorithm is convenient in target detection application; however, it only performs well for the signature of target distributed separately with small variance. Reference [10] proposed an adaptive spectral matched filter (ASMF) for radar target detection using antenna array. It is remarkable that most of the present multispectral or hyperspectral algorithms are applied to the remote sensing and medical applications, in which nonstrict demand for real-time and computation complexity are required. Thus, a target detection algorithm based on multispectral imagery with mathematical simplicity, tractability and real-time performance for military application is still a hot issue[11-13].

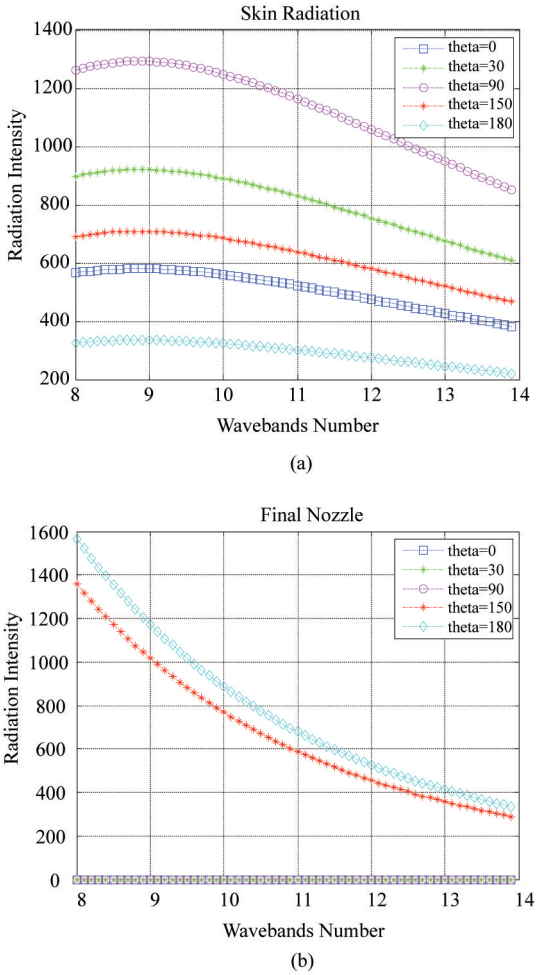

Fig. 1 Radiations in Different Azimuth, (a) Skin thermal radiation, (b) Final nozzie radiation
图 1 不同方位角下的蒙皮(a)与尾喷管(b)辐射光谱

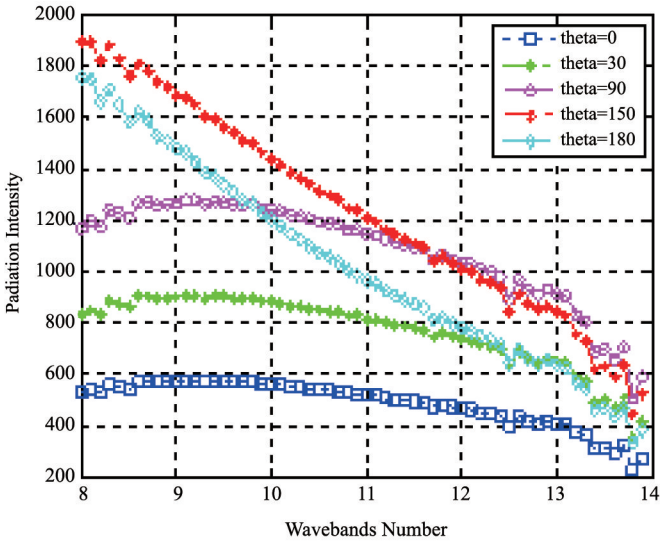

Fig. 2 Total Radiation
图 2 不同方位角下的辐射光谱

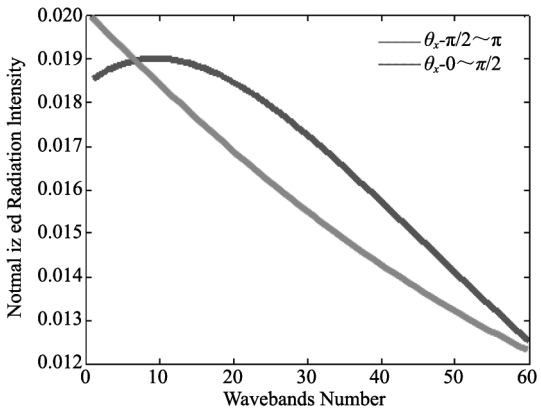

Fig. 3 Spectral model
图 3 不同方位角下的光谱模型

The outline of this paper is organized as follows. In Sec. 1 we present the infrared radiation characteristics of targets and model spectral signature based on concepts and laws of thermal radiation. Sec. 2 describes data cube and image model. In Sec. 3, background removing processing is presented firstly, and then we described the formulation of target detection problem. Finally URIS maximum likelihood ratio statistical decision detector is proposed. Sec. 4 presents a series of simulations to demonstrate the conclusion drawn in Sec. 5.

1 Spectral analysis

In this section, spectral models of target are analyzed. Infrared radiation of aircraft targets can be generally classified into three parts: Final nozzle, Aircraft skin, and Tail flame.

Tail flame radiation is a kind of selective banded spectrum radiation concentrating in 3 ~ 5μm and is negligible in 8 ~ 14 μm. Tail flame radiation characteristic al-

ways changes along with the flight altitude, working states of engine, etc.

Final nozzle is a cylindrical cavity heated by exhausted gas and can be seen as a gray-body with emissivity $\varepsilon_n = 0.9$ in engineering calculation. The spectral radiant existence of the final nozzle is modeled as:

$$Mn_\lambda = \varepsilon_n M_{\lambda bb}(T_n, \lambda) \quad , \quad (1)$$

where, (i): T_n final nozzle temperature; (ii) λ: wavelength; (iii) $M_{\lambda bb}$: Planck's black body function;

Surface temperature is determined by air temperature, airflow pattern and flight Mach number, and can be calculated with the following function:

$$T_s = T_0\left[1 + k\left(\frac{\gamma-1}{2}\right)Ma^2\right] \quad , \quad (2)$$

where, T_s is surface temperature, T_0 is air temperature, k is recovery factor, γ is ratio of heat capacity at constant pressure and constant volume, usually $\gamma = 1.3$, Ma is flight Mach number. Skin thermal radiation can be simply modeled as a gray-body with emissivity ε_s, the spectral radiant existence is described as follows:

$$Ms_\lambda = \varepsilon_s M_{\lambda bb}(T_s, \lambda) \quad , \quad (3)$$

In conclusion, final nozzle thermal radiation and aircraft skin thermal radiation can be approximated as gray body continuous spectrum radiation, and the radiation of tail flame is negligible in 8 ~ 14 μm. Therefore, the aircraft target radiation can be described as a stable gray body radiant model in long-wave band. In a different observation angle, the spectral signature of the aircraft will be different. Then, aircraft targets are considered as Lambert's law radiator whose infrared radiance is:

$$I = M\cos\theta_{az}\cos\theta_{pa}\Delta A/\pi \quad , \quad (4)$$

where, $M = \int Mn_\lambda + Ms_\lambda \mathrm{d}\lambda$, θ_{az} is azimuth, θ_{pa} is angle of pitch, ΔA is target area.

First of all, final nozzle radiation is the main component when observed from the side of rear. Then, when observed from the front, because of the shelter by the aircraft itself, it is weakened to a rather minor constituent. Finally, skin thermal radiation has stable characteristic of all-directions. The spectral curves of final nozzle radiation and skin thermal radiation and in 8 ~ 14 μm band are shown respectively in Fig. 1 with the atmospheric temperature of 288 K, flight altitude of 5 km, angle of pitch 15°, the speed of 1*Ma* and different θ_{az}. Considering the spectral curve distortion caused by atmospheric transmission, the target spectral signatures in different observation angle are modeled as shown in Fig. 2.

Figures 1 and 2 indicate that target signatures varied along with the observation angle which determines the target observation area and radiance emitter. Thus, target spectral curve is merely determined by the kinds of observed radiation emitters and observed target area can only affect the radiance intensity. Thus, based on the difference of observed illuminating source caused by observation angle, normalized target spectral signature models are given in Fig. 3.

2 Date cube and image model

Multispectral data provides not only 2-D image, but also the information in spectral dimension. A single frame is extended to an image cube or data cube with the third dimension specified by spectral wavelengths. L is the number of wavebands for the spectrum, for a pixel, its spectral vector is:

$$X = [x_1 \quad x_2 \quad \cdots \quad x_{(L-1)} \quad x_L] \quad , \quad (5)$$

where x_l is spectral irradiance of l th waveband.

In IR images, pixels can be expressed as:

$$f = t + b + n \quad , \quad (6)$$

in this model, f, t, b and n are the spectral signature of pixels, targets, background and noise. Similar to the traditional Gaussian white noise model, multispectral noise can be presented based on a multidimensional Gaussian distribution. Considering the band-to-band correlation, a first order Markov model is used to generate the covariance matrix defined as follows:

$$C = \sigma^2 R = \sigma^2\begin{bmatrix} 1 & \rho & \cdots & \rho^{L-1} \\ \rho & 1 & & \vdots \\ \vdots & & \ddots & \rho \\ \rho^{L-1} & \cdots & \rho & 1 \end{bmatrix} \quad , \quad (7)$$

R is Toeplitz correlation matrix defined by 1st order Markov model ρ is the band-to-band correlation coefficient σ^2 indicates the dispersion of the noise and the variability of the targets signature, thus varying σ^2 yields different spectral quality.

3 Target detection algorithm

Based on the data cube structure, an integral target detection algorithm scheme is proposed as follows: Firstly, suppress background adaptively. Then, extract gray information and spectral distribution information. Finally, detect targets with detection algorithm proposed in this paper. It is assumed the target information is partly known as prior information, and target signature is modeled by spectral analysis.

3.1 Background removing

Background suppression is aimed at removing slowly varied background which refers to the standard deviation of subimage σ_b is small, specifically $\sigma_b \leqslant 10$ and the subimage is 8×8 pixels in this paper. In background suppression process, our motivation is mainly based on the conclusion that background always performs a significantly correlation in spatial and temporal. Since a single frame image becomes a data cube, thus, the traditional single frame image filter expands to filter bank, each filter in the bank corresponds to a data layer of the data cube, and processing in parallel.

Defining $\bar{h}_l^s$ as spatial mean value and $\bar{h}_l^t$ temporal mean value of a sample pixel in the l th spectral image ($l = 1, 2, \cdots L$), if the area viewed by the pixel is background, as known well, the gray intensity of a pixel h_l can be regarded as a linear combination of $\bar{h}_l^s$ and $\bar{h}_l^t$.

$$h_l \approx \alpha_l \bar{h}_l^s + \beta_l \bar{h}_l^t \quad , \quad (8)$$

where, α_l, β_l are the weights of $\bar{h}_l^s$ and $\bar{h}_l^t$.

Defining $\tilde{h}_l$ as the residual value after background suppression, namely,

$$\tilde{h}_l = h_l - \alpha_l \bar{h}_l^s - \beta_l \bar{h}_l^t \quad , \quad (9)$$

then, the background suppression problem transforms in-

to optimal estimation problem which can be illustrated by the expression:

$$\begin{cases} \overline{\theta} = [\overline{\theta}_1 \quad \overline{\theta}_2 \quad \cdots \quad \overline{\theta}_L] \\ \overline{H} = [\overline{H}_1 \quad \overline{H}_2 \quad \cdots \quad \overline{H}_L] \\ Z = [h_1 \quad h_2 \quad \cdots \quad h_L]^{\mathrm{T}} \end{cases}, \quad (10)$$

where, $\overline{H}_l = [\overline{h}_l^s \quad \overline{h}_l^t]$, $\theta = [\alpha_l, \beta_l]^{\mathrm{T}}$. Obviously, this is a typical linear least square problem, we can obtain:

$$\hat{\theta} = (\overline{H}^{\mathrm{T}}\overline{H})^{-1}\overline{H}^{\mathrm{T}}Z$$

$$\tilde{Z} = Z - \overline{H}(\overline{H}^{\mathrm{T}}\overline{H})^{-1}\overline{H}^{\mathrm{T}}Z \quad (11)$$

Now, the background is suppressed adaptively and the infrared image model (6) is converted to 12 which shows that the residual infrared imagery cube model is now composed of target and noises.

$$f = t + n = N_L(t, C) \quad (12)$$

3.2 Formulation of the problem

Multispectral not only enriches the information but also leads to the calculation complexity and the information confliction. To solve this problem, multispectral information is projected to two fields: radiation intensity and spectral distribution.

In this paper, the standard spectral model could be initialized by the target radiation model described in Sec. 2, as follows:

$$R = [r_1 \quad r_2 \quad \cdots r_{L-1} \quad r_L] \quad (13)$$

As stated above, the multispectral gray vector of a pixel is described as X, spectral angle between X and R denotes the spectral similarity.

$$\varphi(X, R) = \arccos\frac{R \cdot X}{\|R\| \cdot \|X\|} \quad (14)$$

Combining X and $\varphi(X, R)$, the feature vector of sample pixel is defined as follows:

$$V = [\sum_{i=1}^{L} x_i \quad \varphi]^{\mathrm{T}} \quad (15)$$

Generally, target detection and recognition is a typical two class problem, the two hypotheses that the detector must distinguish are given by:

$$H_i|_{i=0,1}: V = [h \quad \varphi]^{\mathrm{T}}, E_i(V|H_i) = (m_{h_i} \quad m_{\varphi_i})^{\mathrm{T}} \quad (16)$$

where, H_0 is noise-only hypothesis, H_1 for target present hypothesis, m_{h_i} *and* m_{φ_i} are the mean value of the intensity and spectrum similarity;

3.3 Target detector

In URIS multispectral statistical detection algorithm, the feature vector of a sample pixel is built as Eq. 15, and then maximum likelihood ratio (MLR) is used to accomplish detecting and recognizing, defining the likelihood ratio test as:

$$\log R = \log\frac{P(V|H_1)}{P(V|H_0)} \quad \log\left(\frac{P(H_0)\lambda_{10}-\lambda_{00}}{P(H_1)\lambda_{01}-\lambda_{11}}\right) \quad (17)$$

where, λ_{ij} is loss function and $\lambda_{11} = \lambda_{00} = 0$.

Figure 4 shows the probability density (PD) distribution of feature vector of the residual image with different ρ. Evidently, this appears approximately Gaussian when ρ is relatively small and increased ρ leads to the distortion to the shape of PD distribution. This phenomenon is derived from the constraint on the spectral correlation of ρ. For mathematical tractability, the samples distribution is approximate to normal distribution. Respectively, the PDFs when the target is absent and present:

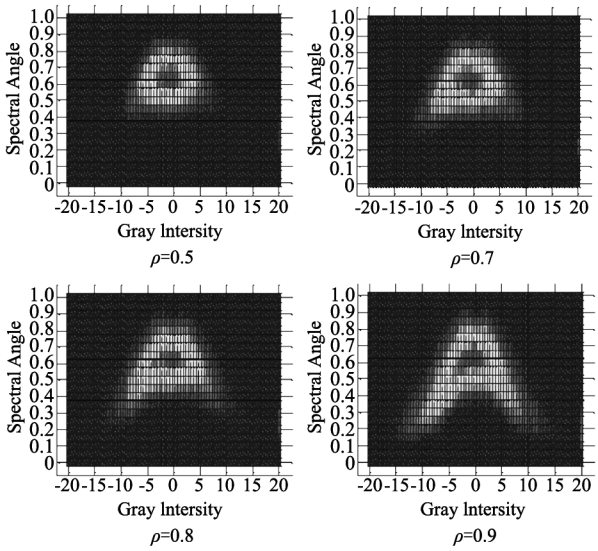

Fig. 4 PD Distribution of Samples
图4 不同谱相关系数下的PD分布示意图

$$P_i(V) = \frac{1}{2\pi|M_i|^{-1}}\exp\left\{-\frac{1}{2}(V-E_i)^{\mathrm{T}}M_i^{-1}(V-E_i)\right\} \quad (18)$$

hence, the test statistic in Eq. 17 reduces to

$$L(V) = \frac{1}{2}[(V-E_0)^{\mathrm{T}}M_0^{-1}(V-E_0) - (V-E_1)^{\mathrm{T}}M_1^{-1}(V-E_1)] \quad (19)$$

$$\text{def: } P = \begin{bmatrix} h-m_{h_0} \\ \varphi-m_{\varphi_0} \end{bmatrix} \quad S = \begin{bmatrix} m_{h_1}-m_{h_0} \\ m_{\varphi_1}-m_{\varphi_0} \end{bmatrix} \quad (20)$$

Substitute Eq. 20 to Eq. 19 and restated it as:

$$L(V) = \frac{1}{2}(P^{\mathrm{T}}M_1^{-1}S + S^{\mathrm{T}}M_1^{-1}P) - \frac{1}{2}(P^{\mathrm{T}}M_1^{-1}P - P^{\mathrm{T}}M_0^{-1}P) - \frac{1}{2}S^{\mathrm{T}}M_1^{-1}S \quad (21)$$

where, $S^{\mathrm{T}}M_1^{-1}S$ is a constant scalar and is irrelevant to the recognizing sample pixels, $P^{\mathrm{T}}M_1^{-1}S$ and $S^{\mathrm{T}}M_1^{-1}P$ are equivalent scalar.

Hence, the maximum likelihood ratio is related to the first two terms of and the test statistic further reduces to:

$$\eta = \frac{1}{2}(P^{\mathrm{T}}M_1^{-1}S + S^{\mathrm{T}}M_1^{-1}P) - \frac{1}{2}(P^{\mathrm{T}}M_1^{-1}P - P^{\mathrm{T}}M_0^{-1}P) \quad (22)$$

Besides, the expansions of the two terms are given as follows:

Defining matrix N and Q as:

$$N = M_1^{-1} = \begin{bmatrix} N_{11} & N_{12} \\ N_{21} & N_{22} \end{bmatrix}; Q = M_0^{-1} = \begin{bmatrix} Q_{11} & Q_{12} \\ Q_{21} & Q_{22} \end{bmatrix} \quad (23)$$

hence, substitute Eq. 23 in to the first term of Eq. 22, we get:

$$\frac{1}{2}(P^{\mathrm{T}}M_1^{-1}S + S^{\mathrm{T}}M_1^{-1}P) = N_{11}(m_{h_1}-m_{h_0})[(h-m_{h_0}) + N_{11}^{-1}N_{21}(\varphi-m_{\varphi_0})] + N_{22}(m_{\varphi_1}-m_{\varphi_0})[(\varphi-m_{\varphi_0}) + N_{22}^{-1}N_{12}(h-m_{h_0})] \quad (24)$$

Using the fact that:

$$N_{22}^{-1}N_{21} = -K_{h_1h_1}^{-1}K_{h_1\varphi_1}; N_{11}^{-1}N_{12} = -K_{\varphi_1\varphi_1}^{-1}K_{h_1\varphi_1}$$

Then, Eq. 24 can be expressed as:

$$\frac{1}{2}(P^{\mathrm{T}}M_1^{-1}S + S^{\mathrm{T}}M_1^{-1}P) =$$
$$N_{11}(m_{h_1}-m_{h_0})[(h-m_{h_0})-K^{-1}_{\varphi_1\varphi_1}K_{h_1\varphi_1}(\varphi-m_{\varphi_0})]$$
$$+ N_{22}(m_{\varphi_1}-m_{\varphi_0})[(\varphi-m_{\varphi_0})-K^{-1}_{h_1h_1}K_{h_1\varphi_1}(h-m_{h_0})] \quad ,(25)$$

Similarly, the second term of Eq. 22 can be written as:

$$\frac{1}{2}(P^{\mathrm{T}}M_1^{-1}P-P^{\mathrm{T}}M_0^{-1}P) =$$
$$\frac{1}{2}\{N_{11}(h-m_{h_0})[(h-m_{h_0})-K^{-1}_{\varphi_s\varphi_s}K_{h_s\varphi_s}(\varphi-m_{\varphi_0})]$$
$$+ N_{22}(\varphi-m_{\varphi_0})[(\varphi-m_{\varphi_0})-K^{-1}_{h_sh_s}K_{h_s\varphi_s}(h-m_{h_0})]$$
$$-Q_{11}(h-m_{h_0})[(h-m_{h_0})-K^{-1}_{\varphi_0\varphi_0}K_{h_0\varphi_0}(\varphi-m_{\varphi_0})]$$
$$-Q_{22}(\varphi-m_{\varphi_0})[(\varphi-m_{\varphi_0})-K^{-1}_{h_0h_0}K_{h_0\varphi_0}(h-m_{h_0})]\} \quad ,(26)$$

Equation 25 and 26 is the foremost prominent result in this paper; it reveals the procession procedure of the feature vector for target recognition. For a pixel to be made target decision, the mean value of the related local noise should be removed, and then the gray information and spectral information are filtered and subtracted mutually.

It is also well known that the LMSE of $X-\mu_x$ given $Y-\mu_y$ is defined by $X-\mu_x = K_{xx}^{-1}K_{xy}^{-1}(Y-\mu_y)$, thus the follows description is obtained.

$$\frac{1}{2}(P^{\mathrm{T}}M_1^{-1}S-S^{\mathrm{T}}M_1^{-1}P) =$$
$$= N_{11}(m_{h_1}-m_{h_0})[(h-m_{h_0})-(h-m_{h_0})_1]$$
$$+ N_{22}(m_{\varphi_1}-m_{\varphi_0})[(\varphi-m_{\varphi_0})-(\varphi-m_{\varphi_0})_1] \quad ,(27)$$

$$\frac{1}{2}(P^{\mathrm{T}}M_1^{-1}P-P^{\mathrm{T}}M_0^{-1}P) =$$
$$\frac{1}{2}\{N_{11}(h-m_{h_0})[(h-m_{h_0})-(h-m_{h_0})_1]$$
$$+ N_{22}(\varphi-m_{\varphi_0})[(\varphi-m_{\varphi_0})-(\varphi-m_{\varphi_0})_1]$$
$$-Q_{11}(h-m_{h_0})[(h-m_{h_0})-(h-m_{h_0})_0]$$
$$-Q_{22}(\varphi-m_{\varphi_0})[(\varphi-m_{\varphi_0})-(\varphi-m_{\varphi_0})_0]\} \quad , \quad (28)$$

Thus, substitute Eq. 27 and 28 to Eq. 22, the target decision expression can be presented as:

$$\eta = \eta_1 + \eta_2 + \eta_3 + \eta_4 \quad , \quad (29)$$

where,

$$\eta_1 = N_{11}[(m_{h_1}-m_{h_0})-\frac{1}{2}(h-m_{h_0})][(h-m_{h_0})-(h-m_{h_0})_1]$$
$$\eta_2 = N_{22}[(m_{\varphi_1}-m_{\varphi_0})-\frac{1}{2}(\varphi-m_{\varphi_0})][(\varphi-m_{\varphi_0})-(\varphi-m_{\varphi_0})_1]$$
$$\eta_3 = \frac{1}{2}Q_{11}(h-m_{h_0})[(h-m_{h_0})-(h-m_{h_0})_0]$$
$$\eta_4 = \frac{1}{2}Q_{22}(\varphi-m_{\varphi_0})[(\varphi-m_{\varphi_0})-(\varphi-m_{\varphi_0})_0]$$

Each term in the algorithm description Eq. 29 is firstly whitened followed by subtraction of the mean value and optimal LMSE. This therefore is an alternative interpretation for the contribution of the spectral distribution information to target detection and recognition.

4 Simulation

In this paper, the input data is raw multispectral cube with the spatial resolution of 256 × 256 pixels and the spectral resolution of 13 bands in 8 ~ 14 μm with an interval of 0.5 μm. In practice, due to the limitation, it is difficult to obtain multispectral imagery that contains real targets in low-probability target detection scenarios. An alternative is inserting simulated targets in acquired real spectral imagery with $\rho = 0.85$. We simulate the diffraction effect in the process of infrared system imaging and image an infrared point target as a dispersion spot, called "Airy spot". Moreover, the size of the Airy spot r is determined by the wavelength of the target radiation $\lambda_{\max}$ and the aperture of optical system D as follows:

$$2\sqrt{2}r = 1.2\lambda_{\max}/D \quad , \quad (30)$$

As above, the image of point target images is a convex hull. Figure 5 illustrates the shape of an inserted dim point target which occupies 8 × 8 pixels after dispersion in our simulation.

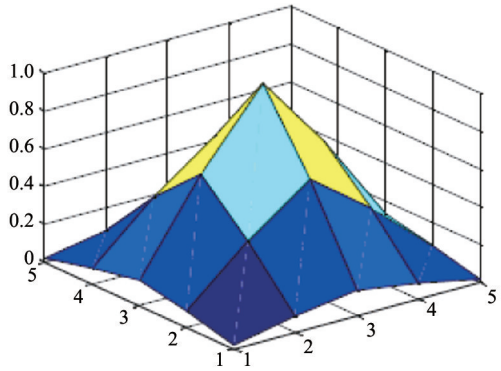

Fig. 5　Dispersed point target
图 5　弥散点目标示意图

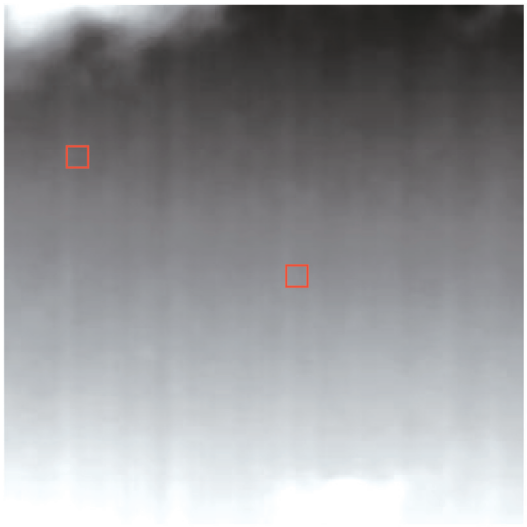

Fig. 6　Original image
图 6 原始图像示例图

Generally, SNR is used to evaluate the image quality and describe the difficulty of dim point target detection. In this paper, for multispectral image assessment, SNR_image evaluating image quality is denoted as:

$$\mathrm{SNR\_image} = \sum_{i=1}^{L}|s_i-\mu_{bi}| \Big/ \sqrt{\sum_{i=1}^{L}\sigma_{bi}^2 + 2\rho\sum_{i<j}\sigma_i\sigma_j} \quad , \quad (31)$$

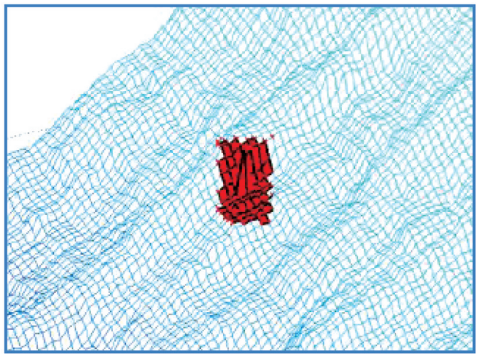

Fig. 7 Partial enlarged image
图 7 目标方位局部示意图

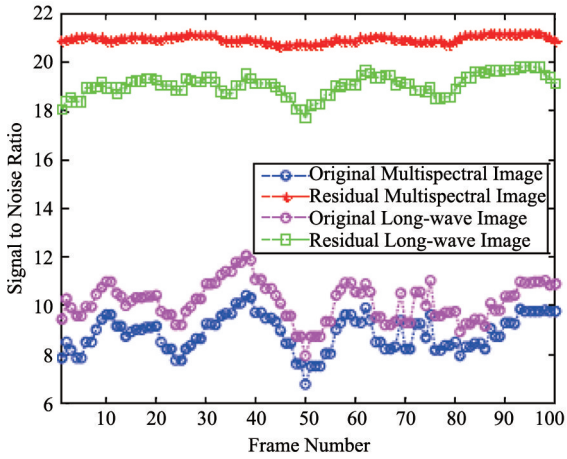

Fig. 8 SNR_image enhancement by removing background
图 8 背景抑制后图像信噪比

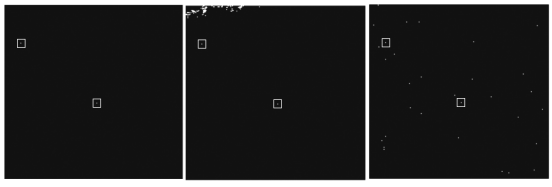

Fig. 9 Target detection results of a single frame with different methods (a) URIS, (b) RI, and (c) SAM
图 9 不同方法单帧图像检测结果(a) URIS, (b) RI, (c) SAM

where, μ_{bi} and σ_{bi} are the mean value and standard deviation of the background in the neighborhood around the target, ρ is the band-to-band correlation coefficient defined in Eq. 7.

In addition, for multispectral imagery, target signature presented as $t = (t_1, t_2, \cdots, t_L)$, and then SNR for evaluating the image quality in spectral perspective is defined as follows:

$$\text{SNR\_sptra} = \sqrt{\frac{1}{L}\sum_{i=1}^{L} t_i^2}/\sigma \quad , \quad (32)$$

where, σ is defined as in expression and varied σ to adjust spectral variability, namely spectral quality.

In this paper, simulation images sequence contains two inserted dim point targets with a background including varying clutter and huge mass of clouds in a cloudy weather condition. Figure 6 gives an example frame to be processed. It is an original multispectral infrared image at wavelength 9 μm which corresponds to the strongest target radiation. As shown in the figure, targets are so small and dim that almost cannot be distinguished. Figure 7 shows the details of the enlarged image, dim point targets in the shape of convex hull are visible.

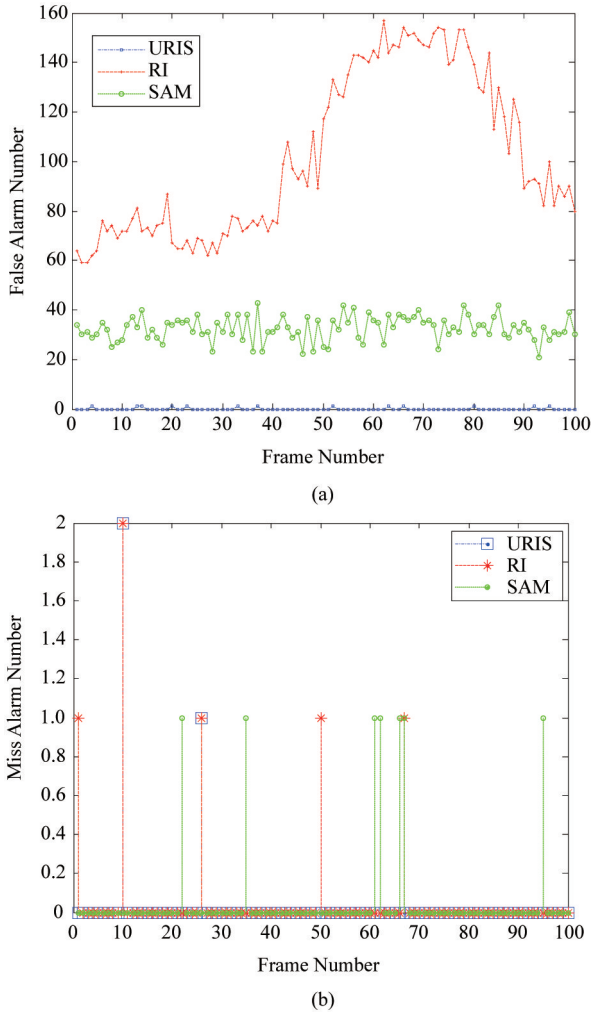

Fig. 10 False alarm (a) and miss alarm (b) statistical results
图 10 连续帧图像 (a)虚警统计, (b)漏警统计

The goal of background suppression is removing slowly varied background to enhance the image quality. Figure 8 shows the SNR_image enhancement of multispectral imagery sequence and corresponding signal-band long-wave images in 100 frames. The result indicates that the background suppressing improves the images quality effectively. Besides, multispectral background suppression has a superior performance for ordinary long-wave images.

Our methed was compared with MLR method based on only radiation intensity (RI) and SAM maximum likelihood ratio statistical approach (SAM). Considering the tradeoff between algorithm performance and mathematical

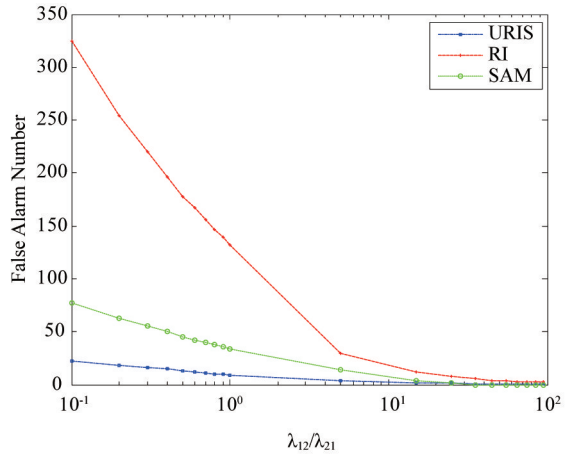

(a) False alarm

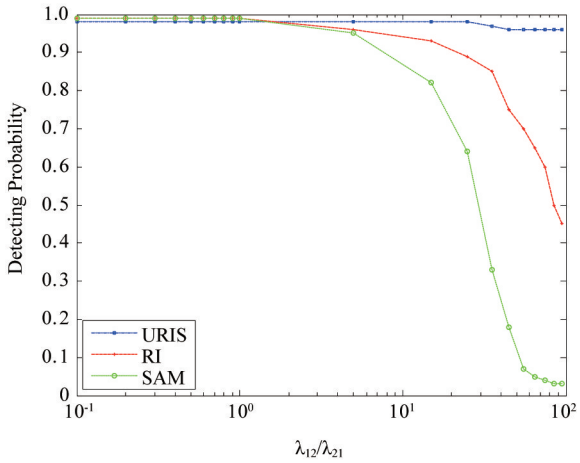

(b) Detectionrobability

Fig. 11　Performances to different loss function$\lambda_{10}/\lambda_{01}$ (a) False alarm, (b) Detectionrobabililty

图 11　不同损失函数下算法性能分析(a)虚警数，(b)检测概率

tractability a large spectral image of 256 × 256 pixels was divided into 1024 small 8 × 8 pitches. Then, estimations for mean vectors and covariance matrix were made in each subimage.

Firstly, target detection results derived with the there methods are shown in Fig. 9. It illustrates that the performance of URIS is much better than other two algorithms. These results demonstrate that introducing multispectral information to target detection is significantly to improve the detection algorithm performance.

Secondly, Fig. 10 shows the false alarm and miss alarm number statistical results of the applied methods, and reveals that URIS method effectively decreases false alarm (about 99.87% for RI and 99.60% for SAM) without reducing detection probability. The real-time performance at MATLAB environment with general-purpose computer is evaluated in Table 1. The time consuming of URIS increases in an acceptable range where 15.82% for RI and 22.03% for SAM.

Table 1　Time consuming statistic

表 1　实时性统计

Methods	Average computing time per frame (s)
URIS	4.308
RI	3.720
SAM	3.531

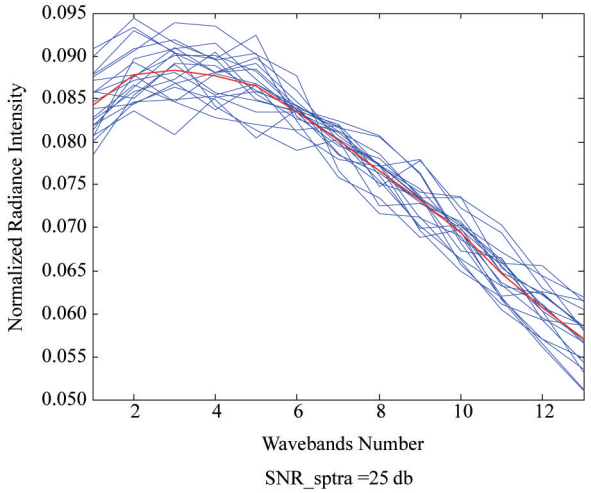

SNR_sptra =25 db

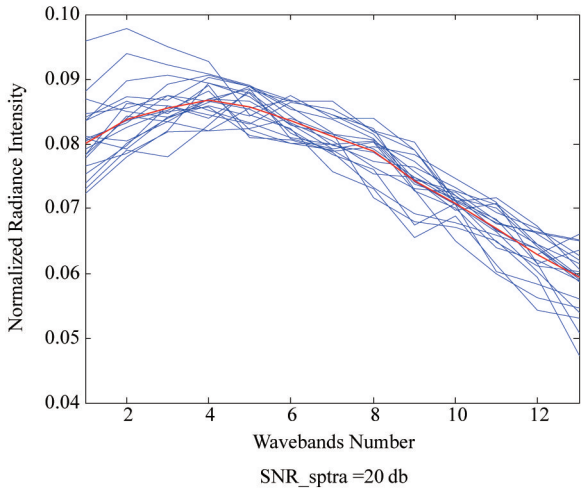

SNR_sptra =20 db

Fig. 12　Spectral variability with different SNR_sptra

图 12　不同光谱信噪比对光谱影响

For the purposes of testing the ROC performance, 100 targets were inserted in each of frames and its spectral signature is "corrupted" with different SNR_sptra. Figure 12 shows spectral variability of the corrupted targets with different SNR_sptra. The randomly selected locations of the targets are fixed for all scenes. The ROC curves of different methods with different spectral variability and image quality are shown in Fig. 13 and Fig. 14 respectively. As shown in Fig. 13, SAM is sensitive to spectral variability aggravation. However, our algorithm still performs well when spectral signature is highly corrupted. As Fig. 14 shows, when SNR_image was decreased, RI results an apparent deteriorating performance over detection target. By comparison, our algorithm shows high performance in resisting image quality degradation.

Finally, Fig. 11 shows the impacts of loss function

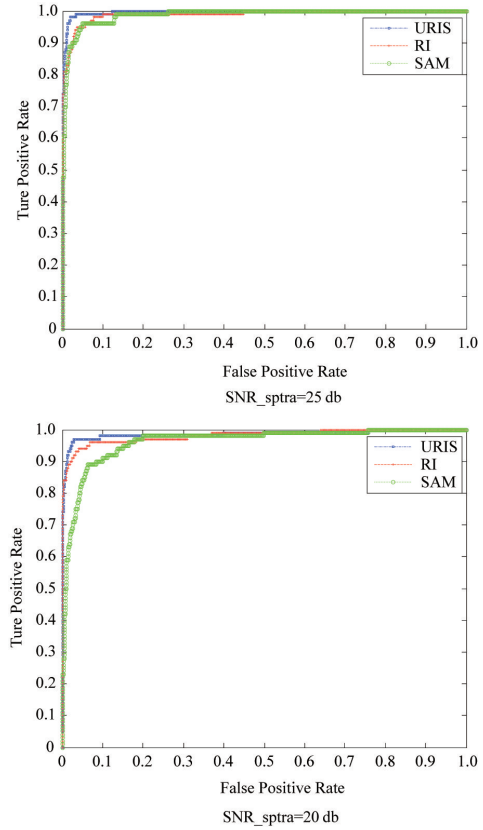

Fig. 13 ROC Curves with different spectral variability
图 13 不同光谱信噪比下 ROC 曲线分析

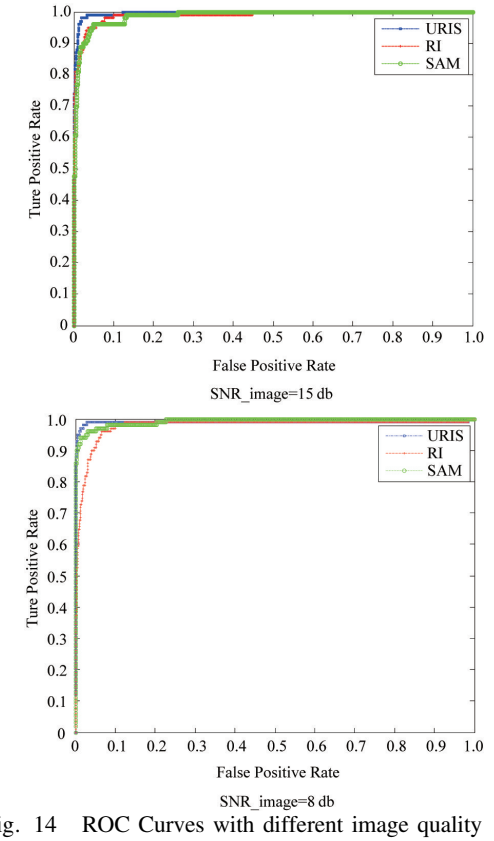

Fig. 14 ROC Curves with different image quality
图 14 不同图像信噪比下 ROC 曲线分析

on algorithm performance. As the $\lambda_{10}\lambda_{01}$ increasing, the false alarm drops sharply. However, for RI and SAM method, the detection probability is also decreasing. URIS shows superior performance on detecting targets and achieving balance between restraining false alarm and detecting targets compared with RI and SAM methods.

5 Conclusions

Based on the previous experimental results, the following conclusions can be drawn from simulation.

First and foremost, URIS performs best among the three methods, reduces false alarm rate greatly without losing detecting probability. This result interprets that introducing spectral information and combing with radiation intensity information are helpful to improve the detection performance.

In this paper, multispectral information is projected to two fields to solve the problem of mathematical calculation and information conflicts. Besides, unifying radiation intensity and radiation spectral signature make the two information compensate mutually, thus the method perform well against the degradation of spectral variability and image quality.

Finally, the approach presented in this paper improves the single image detection performance effectively with mathematical simplicity and tractability. It is significant to establish targets chains to achieve the goal of stable tracking in , and the risk of calculation explosion in target tracking due to the unreliability of single frame detection is reduced.

References

[1] LIU Hong-Ying, LI Qing-Li, XU Liang, *et al*. Evaluation of erythropoietin efficacy on diabetic retinopathy based on molecular hyperspectral imaging (MHSI) system[J]. *J. Infrared Millim. Waves*(刘洪英,李庆利,胥亮,等. 分子超光谱成像系统应用于糖网病疗效研究. **红外与毫料波学报**), 2012, **31**(3):248-253.

[2] Andrew M E, Ustin S L. The role of environmental context in mapping invasive plants with hyperspectral image data[J]. *Remote Sensing of Environment*, 2008, **112**(12): 4301-4317.

[3] Bannari A, Pacheco A, Staenz K, *et al*. Estimating and mapping crop residues cover on agricultural lands using hyperspectral and IKONOS data[J]. *Remote sensing of environment*, 2006, **104**(4): 447-459.

[4] Manolakis D, Siracusa C, Shaw G. Hyperspectral subpixel target detection using the linear mixing model[J]. *Geoscience and Remote Sensing, IEEE Transactions on*, 2001, **39**(7): 1392-1409.

[5] Fan J, Yang J. Trends in infrared imaging detecting technology[C]//*SPIE Security + Defence. International Society for Optics and Photonics*, 2013: 889615-889615-13.

[6] Margalit A, Reed I S, Gagliardi R M. Adaptive optical target detection using correlated images[J]. *Aerospace and Electronic Systems, IEEE Transactions on*, 1985, (3): 394-405.

[7] Reed I S, Yu X. Adaptive multiple-band CFAR detection of an optical pattern with unknown spectral distribution[J]. *Acoustics, Speech and Signal Processing, IEEE Transactions on*,

1990, **38**(10): 1760-1770.

[8] Harsanyi J C, Farrand W H, Chang C I. Detection of subpixel signatures in hyperspectral image sequences[C]//*Proceedings of the American Society for Photogrammetry and Remote Sensing*. 1994: 236-247.

[9] Richards J A, Jia X. *Remote sensing digital image analysis* [M]. Berlin et al.: Springer, 1999.

[10] Robey F C, Fuhrmann D R, Kelly E J, *et al*. A CFAR Adaptive Matched Filter Detector[J]. *IEEE Trans*, 1992, **28**(1).

[11] Yan Y, Liu B. Algorithms of target detection on hyperspectral imagery[J]. *Optik-International Journal for Light and Electron Optics*, 2013, **124**(23): 6341-6344.

[12] Borghys D C, Idrissa M, Shimoni M, *et al*. Fusion of multispectral and stereo information for unsupervised target detection in VHR airborne data[C]//*SPIE Signal Processing, Sensor Fusion, and Target Recognition XXII*, 2013: 874514.

[13] Borghys D C, Kåsen I, Achard V, *et al*. Hyperspectral anomaly detection: comparative evaluation in scenes with diverse complexity[J]. *Journal of Electrical and Computer Engineering*, 2012:160106-16.